KSME Journal, Vol. 7, No. 3, pp. 258~271, 1993

An Experimental Study on the Flow and Heat Transfer Characteristics of an Impinging Jet

Kui-Soon Kim*

(Received February 16, 1993)

The flow and heat transfer characteristics of an impinging jet is investigated in two major stages. The first stage is about the investigation of the three dimensional mean flow and the turbulent flow quantities in free jet, stagnation and wall jet region. After a complete documentation of the flow field, the convective heat transfer coefficient distributions on the impingement plate are presented, during the second stage of the study. Heat transfer experiments using the new hue-capturing technique result in high resolution wall heating rate distributions. The technique is fully automated using a true color image processing system. The present heat transfer results are discussed in detail in terms of the flow characteristics. The measurements from the new method are compared with conventional heat flux sensors located on the same model. These heat transfer distributions are also compared with other studies available from the literature. The new non-intrusive heat transfer method is highly effective in obtaining high resolution heat transfer maps with good accuracy.

Key Words: Impinging Jet, Convection, Liquid Crystal, Image Processing

Nomenclature

c : Specific heat
D : Jet nozzle diameter
H : Distance between the nozzle exit and the impingement plate
h : Convective heat transfer coefficient, $h=q''/(T_w-T_{rec})$
h' : Convective heat transfer coefficient, $h'=q''/(T_w-T_{jmax})$
k : Thermal conductivity
l_n : Jet nozzle length
n : Normal distance from the wall surface
NTSC : National Television System Committee
Nu : Nusselt number, $Nu=hD/k$
Nu' : Nusselt number, $Nu'=h'D/k$
q'' : Heat flux, $q''=-k_f\partial T/\partial n$
r : Radial coordinate
Re : Reynolds number, $Re=\rho U_{jmax}\,D/\mu$

* Department of Aerospace Engineering, Research Institute of Mechanical Technology, Pusan National University, Kumjeong-ku, Pusan 609-735, Korea

R35C1W : Chiral nematic liquid crystal starting to respond at about 35℃ with an approximate bandwidth of 1℃
T : Static temperature
t : Time
U : Mean velocity
u : RMS value of the fluctuating velocity
x : Axial coordinate
α : Thermal diffusivity of air, $\alpha=k/(\rho c_p)$
β : Nondimensional time, $\beta=h\sqrt{t}/\sqrt{\rho ck}$
δ : Difference
θ : Normalized temperature, $\theta=(T-T_i)/(T_{rec}-T_i)$
θ' : Normalized temperature, $\theta=(T-T_i)/(T_{jmax}-T_i)$
μ : Viscosity
ρ : Density

Subscripts

b : Bulk mean
i : Initial condition
j : Jet exit condition

max : Maximum value
p : At constant pressure
rec : Recovery condition
ref : Reference value
w : Wall condition
∞ : Free stream value

1. Introduction

Impinging jets are very attractive in heat transfer augmentation technology. Convective heating or cooling of a selected area of solids can be accomplished effectively with jet impingement because of the high local heat transfer coefficients around the stagnation point. They also show several interesting flow features such as the free jet layer stagnation flow and wall jet layer.

A number of studies investigated the influence of Reynolds number, the distance between the nozzle exit and the impingement plate, and the radial distance from the stagnation point on heat transfer from a heated plate to impinging cold jets (Gardon and Cobonpue, 1962 ; Hrycak, 1983). Obot et al.(1979) found that nozzle geometry influenced mainly the heat transfer coefficient around the stagnation region at small nozzle-to-plate distances. The turbulence level at the nozzle exit was found to affect the heat transfer characteristics by Amano(1983) and Gardon and Akfirat(1965). Striegl and Diller(1984a, 1984b) carried out analytical and experimental studies on the thermal entrainment effect on impinging jet heat transfer. There have been numerous other investigations on impinging jet heat transfer. Reviews of earlier studies on the heat transfer of impinging jets are given in Downs and James(1987) and Martin(1977).

Among the widespread literature on the jet impingement heat transfer phenomena, there are still large differences in distributions of the local heat transfer coefficient, particularly at small nozzle-to-plate distances and in the vicinity of the stagnation point. These discrepancies are caused mainly by the different flow structures of the jets produced by different flow systems. Most of the earlier studies on impinging jets concentrated on the heat transfer results. In this study, the flow field characteristics are investigated for a comprehensive study of the impinging jet flow and heat transfer. The mean velocities and turbulent intensities in the free jet, near the stagnation point and in the wall jet are measured using a five-hole probe and a single sensor hot-wire.

Another objective of this study is to validate the hue-capturing technique as a convective heat transfer measuring tool. The technique which is recently developed by Camci et al.(1992) is a convenient and accurate way of temperature mapping of liquid crystal images. The technique is a true color image processing method whcih is based on color recognition techniques using hue-saturation-intensity description instead of the more widely accepted red-green-blue color definition system. The technique allows the researcher to use many of the visible colors appearing on the liquid crystal coated surface in contrast to many previous methods utilizing only a very narrow, distinct color band which formed a single isotherm. It was concluded that the data density in a typical heat transfer coefficient distribution could be improved about 40 times with the present hardware, compared to the techniques using only a narrow color band as a single isotherm.

A transient heat transfer model, which has never been tried before in impinging jet heat transfer, is devised to obtain heat transfer coefficients through the true color image processing of the liquid crystal images. The heat transfer coefficients are also derived from the temperature history measurements with thin foil K-type thermocouples and compared with the hue-capturing technique results. The hue-capturing technique results are also compared with earlier studies. The measurements are performed for three different Reynolds numbers (Re=30, 000, 40,000 and 50, 000). The effect of the nozzle-to-plate distance is also investigated.

2. Experimental Apparatus and Technique

2.1 Flow system and heat transfer model

The flow system consists of a centrifugal

blower, a settling chamber, a heater, a pipe nozzle and an impingement plate. The air is heated to the desired temperature in the electrical heater section. Then it passes through the nozzle and finally impinges onto the target plate as shown in Fig. 1 The heater section contains a horizontal heater element situated along the centerline of a circular pipe having a 5.08 cm diameter. The heater consists of Nichrome-60 wire of 22 gauge that is wrapped around a Molite refractory ceramic rod of 1.2 cm diameter and 35 cm length. The nozzle section is a PVC pipe of 3.81 cm inner diameter, with a square cut exit section. The length of the pipe is 91.44 cm, resulting in a length to diameter ratio of 24. The distance between the nozzle exit and the impingement plate(H) is adjustable.

Figure 1 shows the schematic of the experimental set-up and the definition of coordinates of the jet flow field. The impingement plate was made of a 19.7 mm thick flat plexiglass plate. The jet side of the plate was coated with a micro-encapsulated chiral nematic liquid crystal layer (Hallcrest, R35C1W). After the application of the crystal layer, a black coating was applied on top of the crystal. The imaging camera was located on the opposite side of the plexiglass model from the jet. This approach provided a viewing angle which was normal to the heat transfer surface. Two incandescent light sources (500 W, 3200℃) were situated on the camera side of the plate to illuminate the heat transfer surface. Four fast response K-type thin foil thermocouples were flush mounted at separate locations on the heat transfer model for calibration purposes. The thermocouples had typical time response of about 5 milliseconds. The uncertainty of the temperature measurement with the thin foil thermocouple was expected to be within $\delta\theta/\theta = \pm 1.9\%$, where θ is defined as $(T_w - T_i)/(T_{rec} - T_i)$. The temperature indicator was located on the camera side of the heat transfer plate. Therefore the video recordings of the liquid crystal image also carried the instantaneous temperature information at a local point.

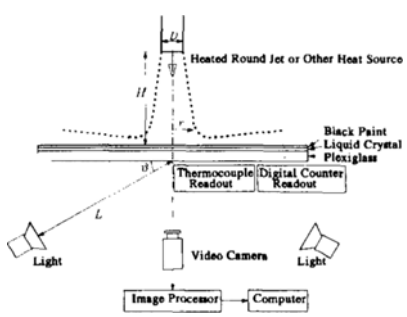

Fig. 1 Experimental set-up

2.2 Flow measurements

A subminiature five-hole probe was employed to obtain the distributions of three orthogonal velocity components, stagnation pressure and static pressure. The probe was fabricated by the Applied Research Laboratory of the Pennsylvania State University as described in Treaster and Yocum(1979). The diamond shaped probe tip had an overall diameter of 1.68 mm and consisted of four holes set 45 degrees off the reference line and the fifth center hole. These five holes provided five pressures to a 48J9-1 Scanivalve system, a pressure sampling scanner. The ouput of the scanner was measured with a ± 0.2 psi range Validyne DP-15 variable reluctance pressure transducer. The measured pressures were relative to atmospheric pressure. A precision U tube manometer was used for the calibration of the pressure transducer. The estimated time response of the transducer was about 1 KHz.

The turbulent intensity and mean velocity of the jet flow field were acquired with a single sensor hot-wire probe. The sensor was made of 5 μm tungsten wire with length-to-diameter ratio of approximately 300. The probe resistance was measured to be 3.49 Ω at 20℃. An AN-1003 hot-wire/hot film anemometer system manufactured by A.A. Lab Systems was used to operate the hot-wire at constant temperature. The operating resistance was set at 1.7 times the measured cold resistance.

2.3 Color definition and the hue-capturing system

Color perception is a psychophysical phenomenon which results from the human eye's translation of radiant energy into visual stimuli. Color may be defined as the combination of those characteristics of light that produces the sensations of

hue, saturation and intensity in a normal human observer. Intensity of a color refers to the relative brightness of a color. This quantity represents a total sum of the spectral energy incoming to the eye/sensor, emitted by an object at various wavelengths in the visible electromagnetic spectrum. Hue refers to that attribute of color that allows separation into groups by terms such as red, green, yellow, etc. In the visible spectrum, hue corresponds directlly to the dominant wavelength of the light incoming to the sensor. Saturation refers to the degree to which a color deviates from a neutral gray of the same intensity-called pastel, vividness, etc. Saturation may also be defined as a color purity or the amount of white contained in a specfic color.

These three characteristics, hue, saturation and intensity represent the total information necessary to define and/or recreate a specific color stimulus. Conceptually, hue-saturation-intensity definition of color is highly convenient and appropriate for an image-processing system to be used in the determination of convective heat transfer parameters from a liquid crystal sprayed surface, simply because the temperature of the point of interest is directly related to the hue value of the color displayed at that point (Camci et al., 1992). Since the relative orientation of the liquid crystal is the main controlling parameter for the color (hue, wavelength), a direct relation between the local temperature and the locally measured hue value can be established. The orientation of liquid crystals is altered by the local temperature distribution on the heat transfer surface. Any temperature change at a given point on the liquid crystal covered surface results in a significant change in the local spectral reflectivity of this point, and therefore a color change is sensed by human eye or a visual sensor.

The present color image analysis system consists of a video camera (Sony, V9), a video decoder/encoder (Data translation, DT2869), and a frame grabber (Data translation, DT2871). The video camera captures images from the liquid crystal coated heat transfer surface. The standard NTSC video signals obtained from the video camera are decoded into the separate red, green, and blue signals by the video decoder/encoder. The frame grabber captures the images on the red-green-blue color space for image processing on IBM PC compatible computers. In addition to real-time color capture, the frame grabber performs real time RGB/HSI and HSI/RGB color-space conversion for processing captured images in either the hue-saturation-intensity or red-green-blue domain. Four individual frame buffers each having $512 \times 512 \times 8$ bits of video memory is used for storing intensity, saturation, hue and additional graphics and text information. This HSI/RGB conversion at the output of the four frame buffers provides a real time display of the contents of the buffers on typical RGB or NTSC color monitors. Further details of real time hue capturing process are described in Camci et al. (1992).

2.4 Liquid crystal calibration

A baseline experiment was performed on the liquid crystal coated surface in order to find out the dependency of the liquid crystal color to temperature. The local temperature of the liquid crystal surface was changed by applying a radiative heat flux from a temperature controlled heated plate. An extremely slow varying color pattern and the thermocouple temperature readout were recorded simultaneously. Two sets of color defining parameters including red-green-blue and hue-saturation-intensity at the thermocouple location were obtained at different local temperatures.

Figure 2 shows the details of hue versus temperature relation. The color information in the form of hue shows a very linear variation with respect to local temperature between 35.3℃ and

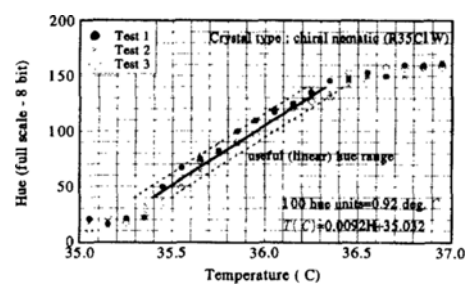

Fig. 2 Hue versus temperature relation

36.3℃. The hue values smaller than 30 represented the "almost black" zone appearing just before red for the specific liquid crystal used, (Hall crest, R35C1W). The hue range between 30 and 140 contained typical colors such as red, orange, yellow, green and blue. This linear range was the most useful part of the hue versus temperature relation in terms of performing accurate temperature measurements using the color-capturing technique. A complete spectrum of colors was located in an almost 1℃ wide temperature band. The discrete data points shown in Fig. 2 showed an uncertainty band of less than ±0.1℃ in the hue range between 30 and 140. However, this uncertainty band was obtained only from data scatter of the hue versus temperature relation. The final uncertainty band of the technique was estimated to be ±0.25℃, since the calibration was performed with a thin foil thermocouple having an uncertainty band of ±0.15℃. The hue values above 140 corresponded to the wide dark blue zone which is very typical of liquid crystal images. The present color image processing system uses an eight bit discretization for the hue-capturing process. This feature allowed division of the complete color range into 256 units. For the specific liquid crystal calibrated, the slope of the useful hue range suggested that a 0.92℃ change in the local temperature corresponded to a relative hue change of 100 hue units.

2.5 Transient heat transfer measurements

Forced convection heat transfer from a heated jet to an impingement plate depends on the temperature rise of the model surface when subjected to a transient convective heating or cooling. The transient technique, reviewed by Schultz and Jones(1973) uses the timewise variation of wall temperature as a measure of the wall heat flux (q_w'') and the corresponding heat transfer coefficient (h). When the model has a low thermal conductivity (k), the wall temperature response is limited to a thin layer near the wall surface and the lateral conduction is very small. Therefore the heat conduction into the model may be assumed to be one dimensional into a semi-infinite medium.

Transient heat transfer into a semi-infinite medium with constant thermal properties is governed by the transient one-dimensional diffusion equation

$$\frac{\partial^2 T}{\partial n^2}=\frac{1}{\alpha}\frac{\partial T}{\partial t}, \tag{1}$$

where α is thermal diffusivity.

The boundary and initial conditions can be stated as follows:

$$q_w''(t)=h(T_w-T_{ref})=-k\frac{\partial T}{\partial n} \text{ at } n=0, \tag{2}$$

$$T=T_i \text{ at } n=-\infty, \tag{3}$$

$$T=T_i \text{ at } t=0, \tag{4}$$

where T_w, T_{ref} and T_i are wall surface temperature at time t, reference temperature (usually constant free stream fluid temperature) and initial wall surface temperature, respectively.

The solution of the above equations relates the wall surface temperature history to heat flux:

$$q_w''(t)=\sqrt{\frac{\rho ck}{\pi}}\left[\frac{T_w(t)}{\sqrt{t}}+\int_0^t\frac{T_w(t)-T_w(\tau)}{(t-\tau)^{3/2}}d\tau\right] \tag{5}$$

In this form there is a singularity in the integral term at $t=\tau$ which will give rise to error in heat flux computation. This error will in general be larger for small t. Numerical integration of the second part of the expression moves the singularity out of the denominator. Jones(1959) recommended a trapezoidal rule to evaluate the integral over the first $(n-1)$ time divisions and a linear temperature-time relation for the last interval.

$$q_{wn}''(t)=\frac{\sqrt{\rho ck}}{\sqrt{\pi}}\left[\sum_{i=1}^{n}\frac{T_w(t_i)-T_w(t_{i-1})}{(t_n-t_i)^{1/2}+(t_n-t_{i-1})^{1/2}}\right] \tag{6}$$

This equation integrates the measured temperature history to give heat transfer coefficients. The temperature histories were measured experimentally with thin foil K-type thermocouples in this study.

Another approach for the measurements of heat transfer coefficient requires additional assumptions. First, the heat transfer coefficient is assumed constant. And if a step change in the fluid temperature is induced, Eq. (1) can be solved to give the surface temperature as

$$\theta=\frac{T_w-T_i}{T_{ref}-T_i}=1-e^{\beta^2}erfc\beta \tag{7}$$

where β is nondimensional time defined as $\beta=(h/k)\sqrt{\alpha t}$. Then, a single measurement of surface temperature at a certain time enables the heat transfer coefficient to be found when the reference temperature, initial temperature and the thermal properties are known.

In the present experiments, the impingement plate material chosen was acrylic which has low thermal conductivity. A thermophysical triple product $\sqrt{\rho ck}$ of 569 $W(s)^{1/2}/(m^2K)$ was used in the data reduction with the uncertainty band of $\pm$ 5% as reported by Baughn et al.(1986). Initially the plate temperature was kept constant at room temperature and the heated jet was diverted by a flow diverter consisting of a removable 90 degree elbow section. The flow diverter was used to guarantee no influence of the heated jet on the uniform initial temperature distribution of the impingement plate. With the removal of the flow diverter, the heated jet suddenly impinged on the plate. The room temperature and the jet maximum temperature was kept near 23℃, and 50 ~60℃, respectively. A liquid crystal layer coated on the model surface was used to monitor the surface temperature. As the model surface temperature changed, a band of color moved across the surface. If the model were initially isothermal, the band of constant color would represent a line of constant heat transfer coefficient. Then the measurements of required times to reach the known color display temperature would allow the solution of Eq. (7) for the heat transfer coefficients. A polynomial curve fitting routine was developed for the variation of the non-dimensional time β with respect to the nondimensional wall temperature θ from Eq. (7). The final form of a sixth order representation used in reducing the liquid crystal image data is as follows;

$$\beta=-0.01071+1.1139\theta-0.66474\theta^2+2.2207\theta^3+8.9339\theta^4-24.571\theta^5+20.586\theta^6 \quad (8)$$

3. Flow Field Surveys and Discussion

This section describes the experimental results of the flow field characteristics of a heated axisymmetric round jet impinging on a normal plate. The mean velocities and turbulent intensities were measured using a five-hole probe and a single sensor hot-wire. The measurements were performed for three Reynolds numbers, $Re=30,000$, 40,000 and 50,000. Another measurement parameter was the ratio of the distance from the nozzle exit to the impingement plate (H) to the nozzle exit diameter (D). The measurements were carried out for $H/D=2$, 4, 6 and 8. The effect of the variation in these parameters has been characterized.

Figure 3 shows the velocity vector distributions measured with the five-hole probe for $Re=30,000$ and $H/D=8$. In this figure, the flow pattern can be subdivided into three characteristic regions: the free jet region, the stagnation flow region, and the wall jet region. Immediately on leaving the nozzle, the air in the jet starts to entrain the surrounding still air. By an intensive exchange of momentum, the jet spreads continuously up to a limiting distance where the mixing region is wide enough to penetrate to the centerline of the jet. The velocity profiles within the potential core like region are relatively unaffected by mixing and are similar to the nozzle exit velocity profile. Beyond the potential core like region the jet decays rapidly as the jet shares its momentum with more and more entrained fluid. In the stagnation flow region, the flow changes its direction due to a strong adverse pressure gradient. Finally the radial wall jet flow develops along the surface. In general, no significant change in the velocities nondimensionalized by the bulk mean velocity due to Reynolds number variation is observed during the experiments.

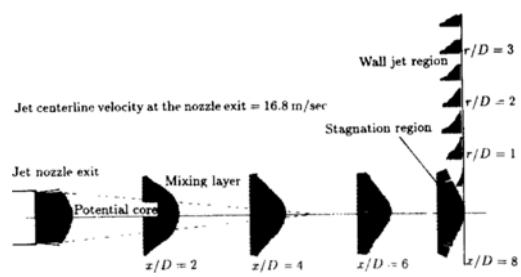

Fig. 3 Jet velocity distributions ($Re=30,000$, $H/D=8$)

Figure 4 shows the axial decay of the centerline mean velocity and the variation of the centerline turbulent intensity for $Re=30{,}000$. When the impingement plate is removed, the centerline mean velocity remains nearly constant ($U/U_b \approx 1.25$) in the potential core like region. The potential core like region is thought to extend to about five nozzle diameters downstream of the nozzle exit. Most prior studies show a potential core like region of five to six nozzle diameters long which is consistent with the present study. The mean velocity suddenly decreases when the mixing layers merge into the centerline beyond the potential core like region ; while, the turbulent intensity of the free jet shows a sharp increase at the end of the potential core like region. With the impingement plate in place, the mean velocity and turbulent profiles follow well those of the free jet without the plate except in the stagnation flow region. In the stagnation region, the mean velocity suddenly drops to zero, while the turbulent intensity shows a significant increase before it drops to zero.

The radial distributions of the mean velocity and turbulent intensity in the free jet region for $Re=30{,}000$, and $H/D=8$ are shown in Fig. 5. The results are plotted as a function of radial distance measured from the jet centerline normalized by the nozzle diameter. Five-hole probe and single sensor hot-wire results agree very well and both characterize the jet spread and decay in Fig. 5(a). The mean velocity at the nozzle exit shows a maximum at the jet centerline and decreases monotonically in the radial direction. The peak values of the turbulent intensity correspond to the nozzle edges, whereas the relative minimum values are related to the jet centerline. Initially, the turbulent intensity peak appears in the center of the mixing region, i.e., at the nozzle radius $r/D=0.5$. This peak is increased dramatically in the early stage of the mixing. However, the centerline turbulent intensity starts to show a significant increase only at the end of the potential core like region. The turbulent intensity levels at the nozzle edge radius are much larger than those of the centerline for $x/D=2$ and 4. Beyond the potential core like region, the turbulent intensity peak located initially at the nozzle radius gradually moves toward the centerline. The turbulent intensity profile is much smoother for $x/D=6$ due to the increase of the centerline turbulent intensity.

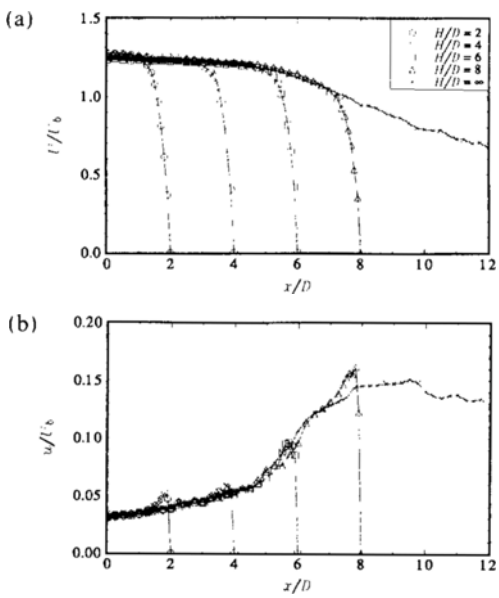

Fig. 4 (a) Mean velocity and (b) turbulent intensity distributions along the jet centerline ($Re=30{,}000$)

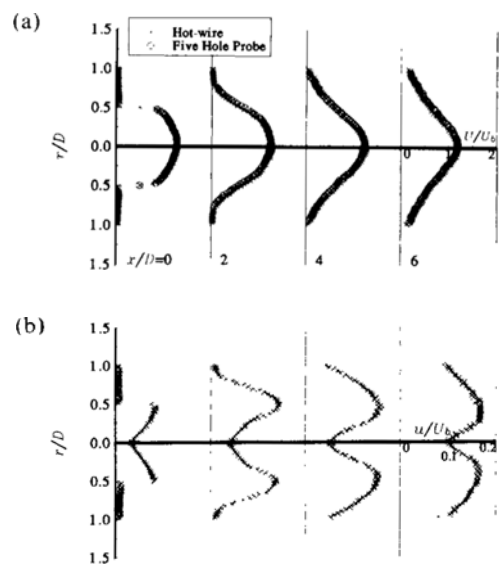

Fig. 5 Radial distributions of (a) mean velocity and (b) turbulent intensity in the free jet region ($Re=30{,}000$, $H/D=8$)

The flow stagnating onto the impingement plate is mixed and highly turbulent. Figure 6 shows the mean velocity and turbulent intensity profiles for $Re=30{,}000$ and $H/D=4$. For this short nozzle-to-plate distance, the potential core like flow of relatively low turbulent intensity stagnates onto the impingement plate.

The total mean velocity distributions in the near wall region are in Fig. 7. The agreement between the five-hole probe and single sensor hot-wire measurements are very good. Since the velocity is zero at the stagnation point, the wall boundary layer grows fast immediately after that point. The mean velocities in the wall layer show maxima around $r/D=1$, then decrease due to diffusion. The wall boundary layer and free jet layer grow together, forming a typical wall jet profile. In the vicinity of the wall, the five- hole probe introduces wall-proximity errors. Considering the agreement with the hot-wire results, this error seems to be negligible in the present measurement range. It should be noted in Fig. 7 that the first five-hole probe measurement location is the third measurement position for the corresponding hot-wire measurements. The wire diameter is of the order of 5 μm. Figure 8(a) shows the

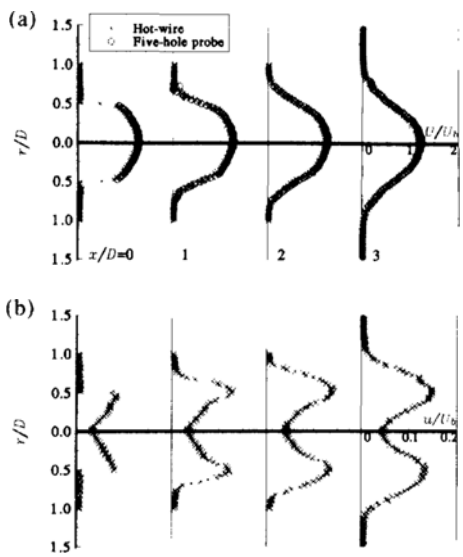

Fig. 6 Radial distributions of (a) mean velocity and (b) turbulent intensity in the free jet region ($Re=30{,}000$, $H/D=4$)

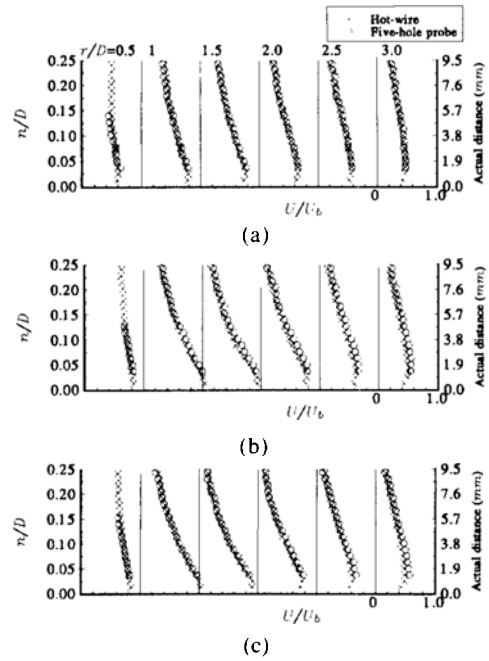

Fig. 7 Mean velocity distributions in the wall jet region, (a) $Re=30{,}000$, $H/D=8$, (b) $Re=30{,}000$, $H/D=4$ and (c) $Re=40{,}000$, $H/D=4$

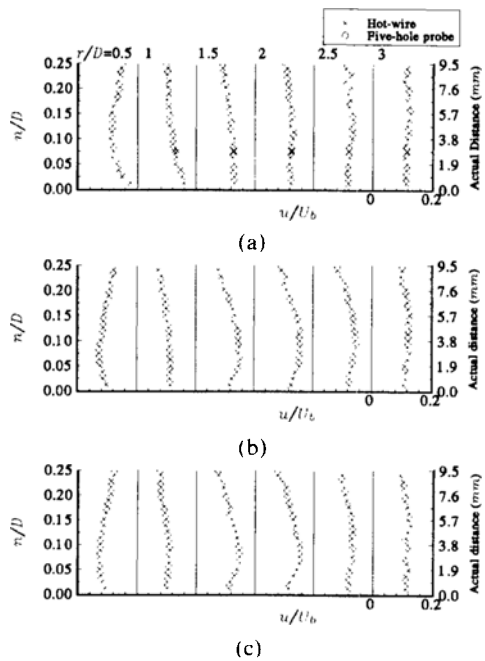

Fig. 8 Turbulent intensity distributions in the wall jet region, (a) $Re=30{,}000$, $H/D=8$, (b) $Re=30{,}000$, $H/D=4$ and (c) $Re=40{,}000$, $H/D=4$

turbulent intensity distribution in the near wall region for $Re=30,000$ and $H/D=8$. Turbulent intensity in the near wall region shows maximum in the stagnation region and monotonically decreases along radial direction. In this case, the fully mixed free jet provides the maximum turbulent intensity at jet centerline before stagnation and the flow of the maximum turbulent intensity hit the stagnation point of the plate. Figures 8(b) and 8(c), which are for $H/D=4$, show quite different characteristics. Turbulent intensity peak appears around $r/D=2$ radial location with the impingement plate at $H/D=4$ for both $Re=30,000$ and 40,000. It has been conjectured that the mixing core region flow of the peak turbulent intensity rapidly diverges close to the impingement plate and meets the plate around $r/D=2$; while, the potental core like flow of low turbulent intensity meets the plate in the stagnation region, resulting in relative minimum turbulent intensity in that region.

4. Heat Transfer Results and Discussion

A very powerful application of the hue-capturing technique is the generation of convective heat transfer coefficients from color images. In this study, the convective heat transfer characteristics of impinging jets are investigated by using the hue-capturing technique based on the transient heat transfer technique described in section 2.5. The heat transfer coefficients are also obtained by fast response thermocouple temperature history measurements for comparison.

The convective heat transfer coefficient is defined as the wall heat flux divided by the difference between the surface temperature and some characteristic temperature of the fluid. Usually the jet maximum temperature is used as the characteristic fluid temperature since it is convenient to obtain. The normalized temperature and the heat transfer coefficients are defined as :

$$\theta'=\frac{T_w-T_i}{T_{j\max}-T_i},\quad h'=\frac{q''_w}{T_w-T_{j\max}},\quad Nu'=\frac{h'D}{k} \tag{9}$$

Another approach is to use the local recovery temperature $T_{\rm rec}$ as the characteristic fluid temperature which results in the following definitions.

$$\theta=\frac{T_w-T_i}{T_{\rm rec}-T_i},\quad h=\frac{q''_w}{T_w-T_{\rm rec}},\quad Nu=\frac{hD}{k} \tag{10}$$

The recovery temperature is defined as the steady state surface temperature at adiabatic conditions.

Goldstein and Behbahani(1982) recommended using the second approach, since the first approach results in the heat transfer coefficient being dependent on heat flux q''. They showed the difference between the two approaches for the jet of uniform temperature identical to the temperature of the surrounding fluid. At a low Reynolds number ($Re=35,200$) when the total temperature in the jet was close to the recovery temperature, there was little difference between the two approaches. But the difference was significant near the stagnation region at high Reynolds number ($Re=121,000$).

The jet exit maximum temperature appears at the jet centerline. It was approximately 60, 55, and 50℃ for $Re=30,000$, 40,000, and 50, 000, respectively, at 23℃ ambient temperature. It is quite obvious that the entrainment of the cold surrounding air to the heated jet tends to cool the jet as they move toward the impingement plate. The heating potential of the jet will be reduced and finally disappear far away from the stagnation region by the cooling effect of the entrained fluid. Thus the heating potential should be considered as the tempeature difference $T_{\rm rec}-T_w$ instead of $T_{j\max}-T_w$, especially for the jet of the nonuniform temperature which is different from the surrounding fluid temperature.

The radial distributions of recovery temperature are measured for $Re=30,000$ in Fig. 9 for various H/D values. The steady state adiabatic condition was achieved after a two-hour continuous run. The recovery temperatures near the stagnation point are nearly the same for both $H/D=2$ and 4, since the potential core like region extends to around five diameters downstream of the nozzle exit. They start to show a small de-

crease at $H/D=6$. The heating potential decreased a lot due to the entrainment of the cold surrounding air at $H/D=6$ and 8. At large distances from the stagnation point, the entrainment effect appears significant even for a very short nozzle-to-plate distance. The recovery temperatures of the wall layer region are relatively smaller than those of the stagnation point. The Reynolds number effect on the recovery temperature distribution was studied in detail. The Reynolds number effect was shown to be negligible.

Figure 10 shows the results of temperature history measurement when the heated jet is suddenly allowed to impinge on the plate. Temperatures are measured through four thin foil K-type thermocouples at 4 separate radial locations from the stagnation points for $Re=30{,}000$ and $H/D=4$. Each temperature profile shows a nearly parabolic increase with time. Local heat flux histories are constructed from the temperature histories with the integral relation given by Eq. (6). Then the heat transfer coefficients are obtained and nondimensionalized by using Eq. (9). The Nusselt numbers shown in Fig. 11 decrease with time at each specific radial location. This tendency indicates that the heat transfer coefficient defined with the jet exit maximum temperature (h') is a function of the value of local heat flux. Nusselt numbers are also obtained through the error function relation, Eq. (7), and compared with the integral relation results. Error function relation, which is used for the data reduction from liquid crystal images, is derived with the assumption of constant heat transfer coefficient. Figure 11 shows that the slight violation of the assumption does not have much effect on the heat transfer coefficient results. The heat transfer coefficients are also computed by using Eq. (10) and plotted in Fig. 12. Nusselt numbers are nearly constant in time during our transient experiment for each radial location. This fact leads us to the conclusion that the actual heating potential is the temperature difference between the local recovery temperature and the wall temperature. And, of course, the heat transfer

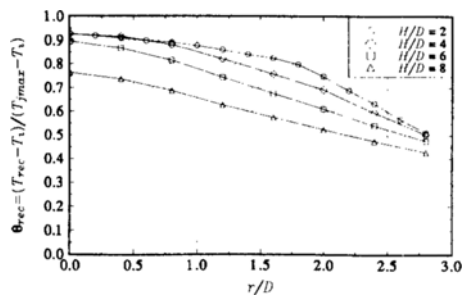

Fig. 9 Radial distributons of recovery temprature ($Re=30{,}000$)

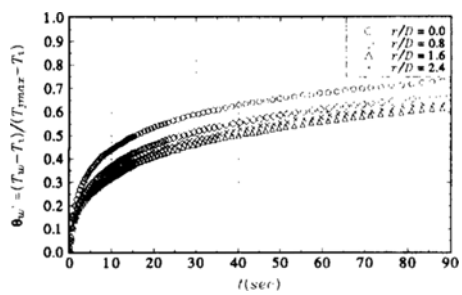

Fig. 10 Temperature histories of the transient heat transfer model measured at 4 separate radial locations

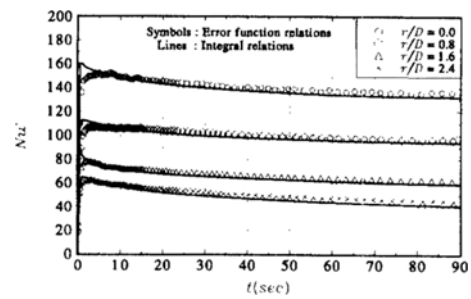

Fig. 11 Nusselt number variations in time obtained from the temperature histories

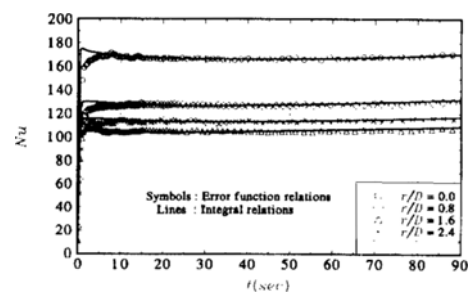

Fig. 12 Nusselt number variations in time obtained from the temperature histories

coefficients defined with the recovery temperature are more universal than those with jet maximum temperature. Integral relation and error function relation results also show an excellent agreement.

Convective heat transfer coefficients are obtained from time stamped color images, using the hue-capturing technique. Figure 13 shows the Nusselt number distribution obtained using 15 individual color images sampled at different times. The first image was captured at $t=7.9$ seconds. from the beginning of the transient experiment and the last image was taken at $t=88.1$ seconds. The multiple temperature points, corresponding to many of the colors which could be captured simultaneously with the present technique, improve the spatial resolution of the final heat transfer coefficient distribution greatly, compared to the previous techniques which provided only one single temperature point per video frame. The presenst method as shown in Fig. 13 provides more than 300 individual heat transfer coefficient measurements by using very accurately calibrated color information assigned to each pixel in the image. The initial wall temperature was uniformly distributed over the plate at an ambient level. The initial wall temperature uncertainty was approximately ± 0.1℃. The elapsed time measurement was performed by using an electronic counter. The time measurement uncertainty was ± 2 milliseconds. The overall uncertainty of the Nusselt number was estimated to be $\pm 5.75\%$ using the standard uncertainty prediction method as described in Appendix. In this figure, the Nusselt number based on jet exit maximum temperature (Nu'), shows much smaller values than the Nusselt number defined by recovery temperature (Nu), especially at large radial distances from the stagnation point. The reason is that the heating potential is decreased much more in the outer region due to the entrainment.

Local Nusselt numbers measured using thermocouples and the new liquid crystal technique are compared in Fig. 14. The hue-capturing technique results agree well for all the radial locations with the thermocouple results based on the integral relation which is known as a reliable method. Liquid crystal tests were performed twice for the same Reynolds number and nozzle-to-plate distance. The liquid crystal results also show an excellent repeatibility.

Local Nusselt number results of the current hue-capturing technique are also compared with the other studies investigated by conventional tools in Fig. 15. Considerable differences in Nusselt numbers exist among those results. This discrepancy may be caused by the differences in the nozzle exit conditions, e. g., the mean velocity profile and the turbulence level. Gardon and

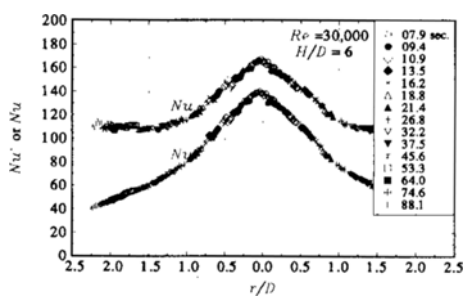

Fig. 13 Nusselt number obtained from 15 different color images

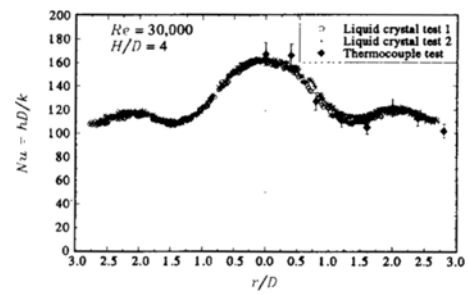

Fig. 14 Radial distributions of Nusselt number ($Re=30{,}000$, $H/D=4$)

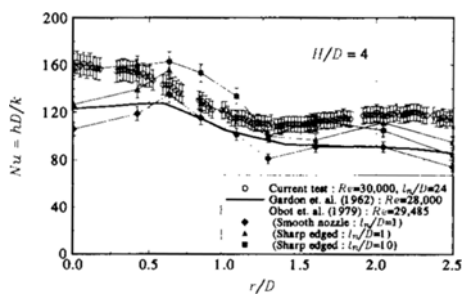

Fig. 15 Radial distributions of Nusselt number

Cobonpue(1962) measured local heat transfer rate of an impinging jet discharged by a nozzle of well rounded inlet and short parallel throat with a steady state heat flux sensor. Obot et al.(1979) obtained heat transfer coefficients through thermocouple measurements of the wall temperature with known constant heat flux. They investigated the effect of the nozzle shape on the flow and heat transfer characteristics of impinging jets. Figure 15 includes the results of Obot et al. from three different nozzle geometries : (1) well contoured inlet, the nozzle length to diameter ratio, $l_n/D=1$; (2) sharp edged inlet, $l_n/D=1$; (3) sharp edged inlet, $l_n/D=10$. They concluded that the difference in nozzle geometry results in different free jet turbulence levels and mean velocity profiles, which in turn affects heat transfer coefficients. And the discrepancy may be attributed to the different temperature conditions. Both previous researches were performed with jets of ambient temperature and heated plate which cause negligible entrainment effect, while our results were obtained with nonuniform heated jet and the plate of ambient initial temperature. However, all the results show a similiar trend with the second peak around two nozzle diameters away from the stagnation point.

Figure 16 shows the effect of the nozzle-to-plate distance on the heat transfer coefficients for $Re=30{,}000$. The overall magnitude of Nusselt numbers show only a slight variation to the distance change due to the nondimensionalization with the recovery temperature. Nusselt numbers decrease monotonically along the radial direction with the maximum at stagnation point for long nozzle-to-plate distance, $H/D=6$ and 8. For $H/D=4$, the second peak in Nusselt number appears around two diameters away from the stagnation point. Sparrow et al.(1975) attributed this to transition from laminar to turbulent flow. The flow around the stagnation point is laminar, since the velocity is zero at the stagnation point. The wall boundary layer grows immediately after that point, and the wall jet flow becomes turbulent. The transition from laminar to turbulent occurs at every nozzle-to-plate distance, since the wall jet layer starts from the stagnation point. But the second peak in Nusselt number appears only at short nozzle-to-plate distances. So the transition can not be the main reason of the second peak in Nusselt number. The second peak in Nusselt number can be attributed to the high near wall turbulent kinetic energy around $r/D=2$ as shown in Fig. 8. Reynolds number effects on heat transfer characteristics are investigated in Fig. 17 for $H/D=4$. The results show significant increase in Nusselt numbers with Reynolds number.

5. Concluding Remark

The hue-capturing technique was implemented for a heated round jet stagnating on a flat wall for the validation of the technique as a laboratory class heat transfer measuring tool. High resolution isothermal mapping was completed in a very time efficient manner. The hue-capturing technique results agreed very well for all the radial locations with the thermocouple results based on the integral relation which is known as a reliable method. The liquid crystal results showed an

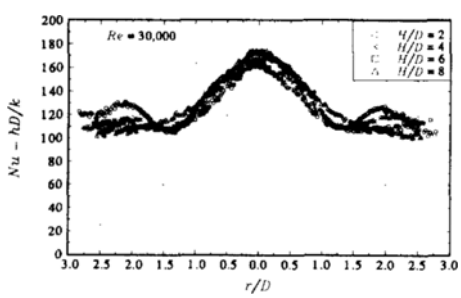

Fig. 16 Nusselt number dependency on $H/D=4$ ($Re=30{,}000$)

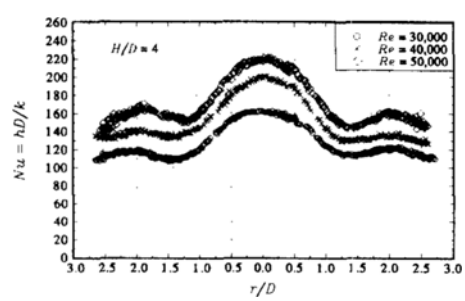

Fig. 17 Nusselt number dependency on Reynolds number ($H/D=4$)

excellent repeatability. Local Nusselt number results of the current hue-capturing technique were also compared with other studies investigated using conventional tools. Differences in Nusselt number existing among those results were caused by the difference of the nozzle exit conditions, e. g., mean velocity profile, turbulence level and temperature conditions. However all the results showed similar trend with the second maximum around two nozzle diameters away from the stagnation point. In general, the results from the hue-capturing technique agreed well with the results available from the literature. The overall uncertainty of convective heat transfer coefficient was estimated to be 5.72%, using standard uncertainty estimation technique.

The overall magnitude of Nusselt number showed only a slight variation to the nozzle-to-plate distance change due to the nondimensionalization with the recovery temperature. Nusselt numbers decreased monotonically along the radial direction with the maximum at stagnation point for long nozzle-to-plate distance, $H/D=6$ and 8. But the second maximum in Nusselt number appeared around two diameters from the stagnation point for $H/D=4$. In addition, the heat transfer coefficients showed significant increase with Reynolds number.

References

Amano, R.S., 1983, "Turbulence Effect on the Impinging Jet on a Flat Plate," Bulletin of the JSME, Vol. 26, No. 221, pp. 1891~1899.

Baughn, J.W., Ireland, P.T., Jones, T.V. and Saniei, N., 1988, "A Comparison of the Transient and Heated-Coating Methods for the Measurement of Local Heat Transfer Coefficients on a Pin Fin," ASME Paper 88-GT-180.

Camci, C., Kim, K. and Hippensteele, S.A., 1992, "A New Hue Capturing Technique for the Quantitative Interpretation of Liquid Crystal Images Used in Convective Heat Transfer Studies," Trans. of the ASME, J. of Turbomachinery, Vol. 114, pp. 765~775.

Downs, S.J. and James, E.H., 1987, "Jet Impingement Heat Transfer-A Literature Survey," ASME Paper 87-HT-35.

Gardon, R. and Akfirat, J.C., 1965, "The Role of Turbulence in Determining the Heat-Transfer Characteristics of Impinging Jets," Int. J. of Heat and Mass Transfer, Vol. 8, pp. 1261~1272.

Gardon, R. and Cobonpue, J., 1962, "Heat Transfer between a Flat Plate and Jets of Air Impinging on It," International Developments in Heat Transfer, pp. 454~460, ASME, New York.

Goldstein, R.J. and Behbahani, A.I., 1982, "Impingement of a Circular Jet with and without Cross Flow," Int. J. of Heat and Mass Transfer, Vol. 25, pp. 1377~1382.

Goldstein, R.J., Sobolik, K.A. and Seol, W.W., 1990, "Effect of Entrainment on the Heat Transfer to a Heated Circular Air Jet Impinging on a Flat Surface," Trans. of the ASME, J. of Heat Transfer, Vol. 112, pp. 608~611.

Hrycak, P., 1983, "Heat Transfer from Round Impinging Jets to a Flat Plate," Int. J. of Heat and Mass Transfer, Vol. 26, pp. 1857~1865.

Jones, J.J., 1959, "Shock Tube Heat Transfer Measurements on inner Surface of a Cylinder (Simulating a Flat Plate) for Stagnation Temperature Range 4100 to 8300°R," NASA TN-D-54.

Kline, S.J. and McClintock, F.A., 1953, "Describing Uncertainties in Single Sample Experiments," Mechanical Engineering, Vol. 75, pp. 3~8.

Martin, H., 1977, "Heat and Mass Transfer between Impinging Gas Jets and Solid Surfaces," Advances in Heat Transfer, Vol. 13, pp. 1~60.

Obot, N.T., Majumdar, A.S. and Douglas, W.J. M., 1979, "The Effect of Nozzle Geometry on Impingement Heat Transfer under a Round Turbulent Jet," ASME Paper 79 WA/HT-53.

Schultz, D.L. and Jones, T.V., 1973, "Heat Transfer Measurements in Short Duration Hypersonic Facilities," AGARD-AG-165.

Sparrow, E.M., Goldstein, R.J. and Rouf, M. A., 1975, "Effect of Nozzle-Surface Separation Distance on Impingement Heat Transfer for a Jet in a Crossflow," Trans. of the ASME, J. of Heat Transfer, Vol. 97, pp. 528~533.

Striegl, S.A. and Diller, T.E., 1984a, "An Ansalysis of the Effect of Entrainment Temperature on Jet Impingement Heat Transfer," Trans.

of the ASME, J. of Heat Transfer, Vol. 106, pp. 804~810.

Striegl, S.A. and Diller, T.E., 1984b, "The Effect of Entrainment Temperature on Jet Impingement Heat Transfer," Trans. of the ASME, J. of Heat Transfer, Vol. 106, pp. 27~33.

Treaster, A.L. and Yocum A.M., 1979, "The Calibration and Application of Five Hole Probes," ISA Transactions, Vol. 18, No. 3, pp. 23~34.

Appendix

The maximum errors in the measurements at better than 95% confidence level are estimated as:

$\delta(T_{rec}-T_i)/(T_{rec}-T_i)$: $\pm 1.5\%$
$\delta(T_w-T_i)/(T_w-T_i)$: $\pm 1.0\%$
$\delta\sqrt{\rho ck}/\sqrt{\rho ck}$: $\pm 5.0\%$
$\delta t/t$: $\pm 1.0\%$
$\delta D/D$: $\pm 0.5\%$
$\delta k/k$: $\pm 0.1\%$

An additional error in $(T_{rec}-T_i)$ caused by the jet temperature fluctuation is added to the measurement error. The error in heat conductivity (k) is calculated from the measurement error in room temperature.

The uncertainty of heat transfer coefficient (h) is the combination of the above listed errors. Kline and McClintock(1953) suggested the following error combination principle.

$$\delta R(v_1, v_2, \cdots, v_n) = [(\frac{\partial R}{\partial v_1}\delta v_1)^2+(\frac{\partial R}{\partial v_2}\delta v_2)^2+\cdots+(\frac{\partial R}{\partial v_n}\delta v_n)^2]^{1/2} \quad (11)$$

With the help of this principle, the uncertainty of the nondimensional temperature, $\theta=(T_w-T_i)/(T_{rec}-T_i)$ is calculated as:

$$\frac{\delta\theta}{\theta}=1.80\%$$

The calculation of the uncertainty of the nondimensional time β is based on Eqs. (8) and (11).

$$\frac{\delta\beta}{\beta}=\frac{1}{\beta}\frac{\partial\beta}{\partial\theta}\delta\theta=2.74\%$$

The combination rule for the heat transfer coefficient uncertainty is obtained from Eq. (7).

$$\frac{\delta h}{h}=[(\frac{\delta\sqrt{\rho ck}}{\sqrt{\rho ck}})^2+(\frac{\delta T}{2t})^2+\left(\frac{\delta\beta}{\beta}\right)^2]^{1/2}=5.72\%$$

Finally the uncertainty of the Nusselt number is obtained as:

$$\frac{\delta Nu}{Nu}=[(\frac{\delta h}{h})^2+(\frac{\delta D}{D})^2+(\frac{\delta k}{k})^2]^{1/2}=5.75\%$$

The main error source in this Nusselt number uncertainty calculation is the measurement error in thermophysical triple product $\sqrt{\rho ck}$. The uncertainty level in Nusselt number can be decreased down to 4.12% by reducing this measurement error of $\sqrt{\rho ck}$ to 3.0%.